Impact of Photogenerated Charge Carriers on the Stability of 2D/3D Perovskite Interface

Zhaojie Zhang[†], *Miu Tsuji*[‡], *Xin Hu*[§], *Tomoyasu Mani*[‡], *D. Venkataraman*[†]*

[†] Department of Chemistry, University of Massachusetts Amherst, Amherst, MA 01003, United States

[‡] Department of Chemistry, University of Connecticut, Storrs, CT 06269, United States

[§] Department of Polymer Science and Engineering, University of Massachusetts Amherst, Amherst, MA 01003, United States

ABSTRACT

An effective strategy to improve the performance and stability of perovskite solar cells is to deposit a 2D perovskite capping layer on the 3D perovskite. However, when exposed to light, small A-site cations in 3D perovskite exchange with the bulky cations in the 2D layer and degrades of the 2D/3D interface. Therefore, to achieve long-term stability in perovskite solar cells, it is important to understand the nature of photogenerated charge carriers that cause cation migrations at the 2D/3D interface. In this work, we fabricated 2D/3D perovskite stacks on glass, ITO, ITO/PTAA, ITO/PTAA/CuI and ITO/SnO_2. A combination of grazing incidence X-ray diffraction, steady-state and time-resolved photoluminescence studies reveals the link between the light-induced

degradation and the photogenerated charge carrier dynamics. Upon illumination, the stability of the 2D layers follows this trend: ITO/PTAA/CuI≈ITO>ITO/PTAA>glass>ITO/SnO_2 (from stable to unstable). This trend suggests that extracting holes efficiently from the 3D layer can improve the stability of the 2D layer. We also found that 2D/3D stacks degrade faster when illuminated from the 2D side instead of the 3D side. Our studies suggest that to achieve a stable 2D/3D interface, hole accumulation in the 3D layer should be avoided and the exciton density in the 2D layer should be reduced.

INTRODUCTION

Ruddlesden-Popper 2D perovskites are often used as capping layers on 3D perovskites to improve the stability and power conversion efficiency (PCE) of perovskite solar cells (PSCs).[1–3] The alignment of the energy levels in the 2D/3D bilayer heterostructures facilitate efficient charge extraction at the 2D/3D interface,[4] which results in higher PCEs in PSCs.[5] The 2D layer can also passivate surface defects of the 3D layer, reduce recombination, prevent moisture uptake, and inhibit volatilization of A-site organic cations from the 3D perovskite, which leads to better stability.[6–8] Many of the best PSCs take advantage of the 2D or quasi-2D perovskite capping layers on top of 3D perovskite.[9–13]

However, the 2D/3D interface could potentially lead to instability issues under illumination and thermal stress. Many studies show that the ion migration at the 2D/3D interface degrades the interface and reduces the PCE.[14,15] Upon heating or under light, the small A-site cations from the 3D perovskite might permeate into the 2D layer and turn the 2D layer into quasi-2D perovskite with high n-values.[16,17] The large spacer cations from the 2D layer might migrate into the 3D layer, create cation vacancies in the 2D layer, and change the composition of the 3D layer.[5] The

trap states in the degraded 2D/3D interface increases recombination rates. As such, the interface becomes a barrier for charge transport to the electrodes.[14,17] Therefore several approaches have been studied to arrest cation migration across the 2D/3D interface. They include engineering the reactivity of the spacer cations[18], inserting a cation-blocking polymer layer between the 2D and 3D layer[4], and improving the phase purity of the 2D layer.[6] While these approaches show some promise, the choices of spacer cations are limited and the fabrication becomes complex , thus limiting scalability.

In PSCs, light is a principal driving force of ion migration.[19] Light can induce halide and cation segregation in mixed-halide or mixed-cation PSCs.[20–23] Photogenerated charge carriers reduce the energy barrier for ion migration, induce defects and accelerate the defect-assisted ion migration.[22,24–27] Thus, delineating how photogenerated charge carriers trigger ion migration at the 2D/3D interface would allow us to stabilize the 2D/3D interface. In this work, we fabricated 2D/3D bilayer perovskite films on various charge transport layers, including poly[bis(4-phenyl)(2,4,6-trimethylphenyl)amine (PTAA), PTAA/CuI bilayer, and SnO_2, and monitored their stability under continuous illumination. We investigated the impact of the underlying charge transport layers on the morphology and composition of the 2D/3D stacks. We illuminated the 2D/3D stacks from either the 2D side or the 3D side and used grazing incidence X-ray diffraction (GIXRD) to monitor the depth-resolved crystallinity change of the 2D and 3D layers under different illumination conditions. We then used steady-state photoluminescence spectroscopy and time-resolved photoluminescence spectroscopy to study the charge carrier dynamics of the 2D/3D bilayer stacks and correlated the photogenerated charge dynamics to the stability of the 2D/3D interface. We found that the choice of hole transport layers (HTL) or electron transport layers (ETL) under the 2D/3D stacks significantly impacts the stability of the

interface. The 2D/3D stacks deposited on HTL, and bare ITO exhibit better stability than those on bare glass while those on ETL have the worst stability. We therefore conclude that the accumulation of holes in the 2D/3D stacks results in fast degradation of the 2D layer. We also found that the incident light direction, which determines the charge carrier photo-generation rate profile in the 2D and 3D layers, plays an important role in the charge carrier dynamics and stability of the 2D/3D interface. Illuminating the 2D/3D stacks from the 3D layer side reduces the exciton photo-generation rate in the 2D layer and improves the stability of the 2D layer. Our work reveals that reducing the photogenerated hole accumulation in the 3D perovskite layer and the photogenerated exciton density in the 2D layer can suppress the cation migration and improve the stability of the 2D/3D interface.

MATERIALS AND METHODS

Materials. The indium tin oxide (ITO)-coated glass substrates were purchased from Kintec Company. PTAA (average M_n 7000-10000), CuI (anhydrous, 99.995%), $SnCl_2 \cdot 2H_2O$ (98%), 2,2,2-trifluoroethanol (TFE) and PMMA were purchased from Sigma-Aldrich. PbI_2 (ultra dry, 99.999%) and KI (99%) were purchased from Thermo Fisher. Methylammonium iodide (MAI) and phenethylammonium iodide (PEAI) were purchased from Greatcell Solar Materials. PCBM was purchased from Nano-C. Tertiary amino-fulleropyrrolidine (C_{60}-N) was purchased from 1-Material. Gamma-butyrolactone (GBL), dimethyl sulfoxide (DMSO), SnO_2 (15 % colloidal solution in water), ethanol, isopropyl alcohol (IPA), acetonitrile, and chlorobenzene (CB) were purchased from Alfa Aesar. Ag pellets (99.99%) for evaporation were from Kurt J. Lesker Company.

Fabrication of 2D/3D perovskite films. Glass and ITO-coated glass substrates were ultrasonicated in soap water, water, acetone, and IPA for 10 min, respectively. PTAA solution was prepared by dissolving PTAA in chlorobenzene (2 mg mL^{-1}). CuI solution was prepared by dissolving CuI (15 mg mL^{-1}) in acetonitrile. The $MAPbI_3$ precursor solution (1.4 M) was prepared by dissolving MAI (225.6 mg), and PbI_2 (677.7 mg with 5% excess) in GBL:DMSO (v:v 7:3). PEAI solution (40 mM) was prepared by dissolving 9.96 mg of PEAI in IPA. PMMA solution (150 mg mL^{-1}) was prepared by dissolving PMMA in chlorobenzene. The PTAA solution was spin-coated on glass or ITO-coated glass substrates at 4000 rpm for 30 s, followed by annealing at 100 °C for 10 min. For PTAA/CuI bilayers, CuI solution was spin-coated on the PTAA layer at 3000 rpm for 60 s, followed by annealing at 100 °C for 10 min. The SnO_2 layer was formed by spin-coating the 2.5% SnO_2 colloidal solution on the glass or ITO-coated glass substrates, followed by annealing at 150° for 30 min. The 3D $MAPbI_3$ layer was formed by spin-coating the $MAPbI_3$ precursor solution. at 1500 rpm for 20 s followed by 2000 rpm for 60 s. 200 μL of chlorobenzene was dropped on the substrate after 40 s. The 3D perovskite films were annealed at 100 °C for 10 min. The 2D perovskite layer was deposited via spin-coating the PEAI solution on the 3D perovskite film at 4000 rpm for 30 s, followed by annealing at 100 °C for 10 min. In the last step, 75 μL of PMMA was spin-coated on the perovskite films at 2000 rpm to provide an encapsulation layer.

Fabrication of PSCs. For the fabrication of PSCs with PTAA or PTAA/CuI as the HTL, PTAA(2 mg mL^{-1}) was spin-coated on ITO-coated glass substrate at 4000 rpm for 30 s, followed by annealing at 100 °C for 10 min. For PTAA/CuI bilayers, CuI solution was spin-coated on the PTAA layer at 3000 rpm for 60 s, followed by annealing at 100 °C for 10 min. The 3D $MAPbI_3$ layer was formed by spin-coating the $MAPbI_3$ precursor solution at 1500 rpm for 20 s followed

by 2000 rpm for 60 s. 200 μL of chlorobenzene was dropped on the substrate after 40 s. The 3D perovskite films were annealed at 100 °C for 10 min. For the 2D layer, the PEAI precursor solution in IPA (4 mM) was spin-coated dynamically on the 3D layer at 4000 rpm for 30 s, followed by annealing at 100°C for 10 min. For the electron transport layer, PCBM (20 mg mL^{-1} in chlorobenzene) was spin-coated on the perovskite films at 2000 rpm for 30 s. Then, C_{60}-N (3 mg mL^{-1} in trifluoroethanol) was spin-coated on PCBM at 4000 rpm for 30 s. Finally, silver was deposited on C_{60}-N by thermal evaporation to form a 100 nm-thick electrode.

J-V measurements. The J-V measurements were conducted under AM1.5G (100mW cm^{-2}) irradiation using a Newport 92193A-1000 solar simulator. J-V scans were obtained from -0.2 to 1.2 V (forward) and 1.2 to -0.2 V (reverse) at a scan rate of 0.12 V s^{-1} using a Keithley 2440 source meter. The average photovoltaic metrics were calculated based on 12 devices.

Grazing incidence X-ray diffraction (GIXRD). GIXRD was measured by a Rigaku SmartLab SE X-ray diffractometer with a Cu Kα source (1.542 Å). The height of the thin film samples was calibrated before each scanning. The incident angle (ω) of the X-ray was set to be 0.2° and 3°, respectively. The 2θ scanning range was from 2.5° to 36° at the speed of 8°/min.

Steady-state photoluminescence spectroscopy and time-resolved photoluminescence spectroscopy (TRPL). The steady-state photoluminescence (PL) was performed by a Horiba Fluorolog-3 spectrometer. The samples were kept in the N_2-filled box and in dark for 1 day before the TRPL measurement. The samples were excited by the 465 nm light from a Xeon lamp with a monochromator. The emission spectrum was collected ranging from 500 to 900 nm. The TRPL was obtained by an Edinburgh FLS1000 Fluorometer using a 405 nm laser (EPL-405,

pulse width ~55 ps) as the excitation source. The emission lifetimes were determined by reconvolution fits using the experimentally measured instrument function (IRF).

Scanning electron microscopy (SEM). The cross-sectional SEM images were obtained by an FEI Megellan field-emission electron microscope with 15 kV accelerating voltage. The samples were prepared by scribing the glass substrates on the back and subsequently splitting the glass substrates to expose the cross-section.

Energy-dispersive X-ray spectroscopy (EDS). EDS was performed by an Apreo VolumeScope SEM with varied acceleration voltage to probe the elemental distribution of Cu and K at the top of ITO/PTAA/CuI/3D and ITO/SnO_2-K/3D, respectively.

RESULTS AND DISCUSSION

To study the impact of various charge transport layers on the stability of the 2D/3D interface, we deposited $MAPbI_3$ on bare substrates (glass or ITO-coated glass), and on ITO substrates coated with the hole transport layer (PTAA, PTAA/CuI) or electron transport layer (SnO_2). We then added a 2D capping layer by spin-coating a solution of PEAI on the 3D $MAPbI_3$ and annealed the films at 100 °C. To minimize the effect of ambient moisture or air, we deposited a layer of PMMA layer on top of the 2D layer.

To investigate the impact of the underlying HTL and ETL on the perovskite films' morphology, we used SEM and AFM to image the morphology of the 3D and 2D/3D stacks. As shown in Figure S1, all 3D layers exhibited complete coverage without any pinholes. Notably, the 3D perovskite film on ITO/PTAA/CuI showed a larger average grain size (315.6 nm) compared to those on glass (241.1 nm), ITO (214.1 nm), ITO/PTAA (255.5 nm), and ITO/SnO_2

(284.2 nm). Root mean square (rms) roughness values calculated from AFM images (Figure S2) indicated that the 3D perovskite films on ITO/PTAA (19.61 nm) and ITO/PTAA/CuI (20.25 nm) were rougher compared to those on glass (17.11 nm), ITO (16.76 nm), and SnO_2 (16.18 nm). SEM images of the 2D/3D stacks indicated the formation of a complete and smooth 2D layer (Figure S3), with all 2D layers exhibiting a similar rms roughness of approximately 23-25 nm (Figure S4).

The underlying HTL and ETL may introduce impurities into the 3D perovskite layer, potentially altering its composition and affecting its stability. In the case of ITO/SnO_2/3D/2D, the SnO_2 ETL was fabricated using the commercial SnO_2 colloidal solution from Alfa Aesar, which contains KOH as a stabilizing agent.[28] This could potentially introduce K^+ ions into the 3D perovskite layer. While some studies have reported that potassium salts, such as KI[29,30], KNO_3[31] and KCl[32], can passivate defects in perovskite films, leading to enhanced performance and stability, it was also reported that KI additives reduce the stability of triple-cation PSCs. [33] For the ITO/PTAA/CuI/3D/2D structure, it is possible that Cu^+ ions from the CuI layer could migrate into the 3D perovskite, passivating cation vacancies and thereby affecting the 3D perovskite composition. If K^+ or Cu^+ ions accumulate at the top surface of the 3D layer, they could also impact the formation of the subsequent 2D capping layer and the ion migration at the 2D/3D interface. We characterized the distribution of K^+ and Cu^+ in the 3D perovskite films deposited on ITO/SnO_2 and ITO/PTAA/CuI using energy-dispersive X-ray spectroscopy (EDS). We increase the accelerating voltage of the electron beam from 4 kV to 9 kV to obtain a qualitative depth profile of the distribution of K and Cu. For the ITO/SnO_2/3D sample, EDS data showed that at an accelerating voltage of 4 kV, no peaks associated with K were observed (Figure S5 and Table S1). At higher voltages (6 kV, 7 kV, 8 kV, and 9 kV), K percentages were

measured to be 1.9%, 1.7%, 3.0%, and 8.0%, respectively, while Sn percentages were 0.9%, 1.1%, 2.0%, and 4.4%, respectively (Figure S5 and Table S1). These results suggest that K^+ is not present at the immediate top surface but may be present deeper in the sample. The co-existence of peaks associated with K and Sn indicates that the K^+ is associated with SnO_2 layer. For the ITO/PTAA/CuI/3D sample, EDS data showed that at an accelerating voltage of 4 kV, no Cu was detected, while at higher voltages (6 kV, 7 kV, 8 kV, and 9 kV), Cu percentages were measured at 0.5%, 0.5%, 1.1%, and 0.8%, respectively (Figure S6 and Table S2). This pattern suggests that Cu^+ is not concentrated at the immediate top surface but may be distributed within the bulk of the film. We note that the resolution of EDS is limited and cannot be used for quantitative depth profiling across ~400 nm perovskite layer. The EDS data conclusively shows the absence of K^+ and Cu^+ at the top surface. Therefore, we conclude that even though they are present in the charge transport layer, they do not get incorporated at the 2D/3D interface.

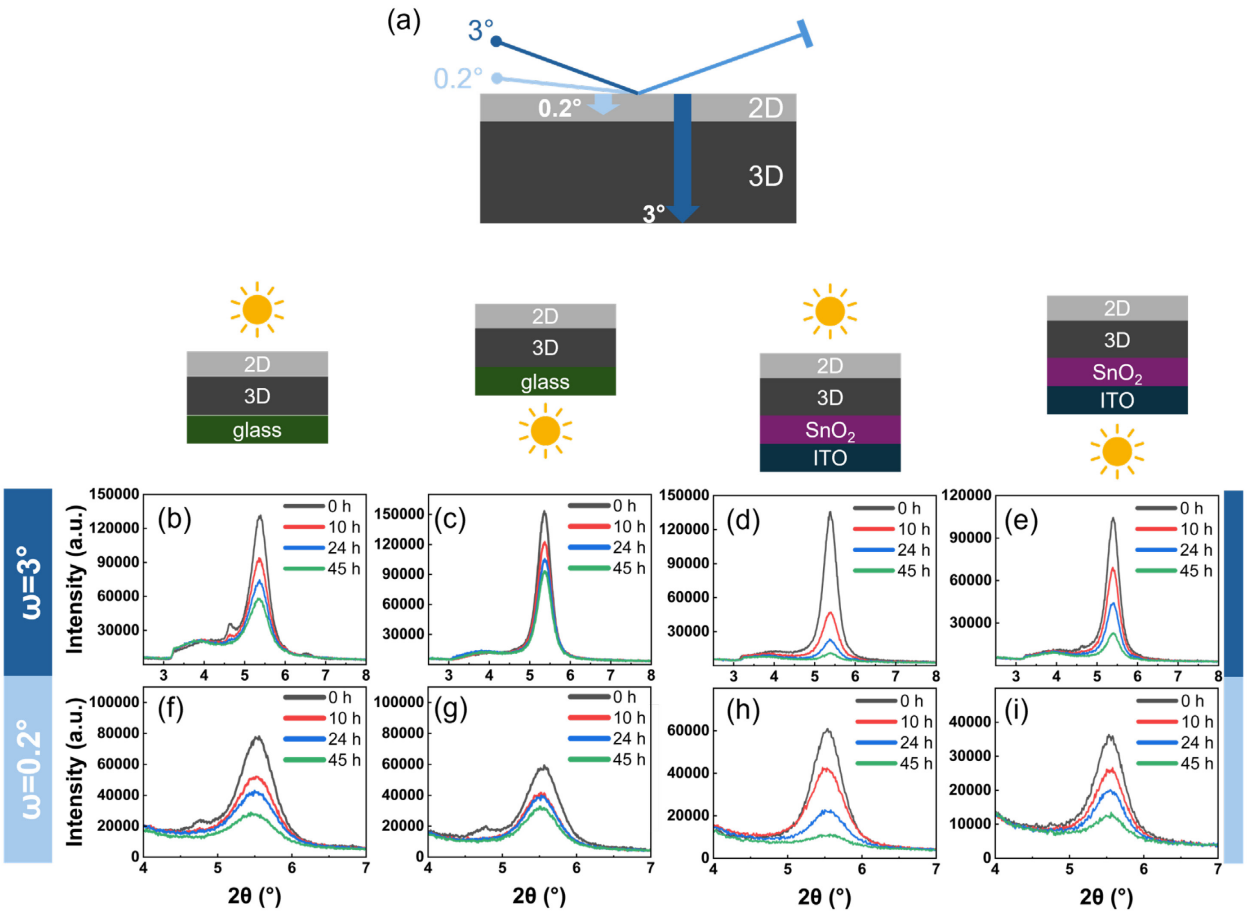

Figure 1. (a) Schematic representation of the penetration depth of the grazing incidence X-rays with ω=3° and ω=0.2°. GIXRD patterns of glass/3D/2D under (b, f) top illumination and (c, g) bottom illumination. The intensities of the (020) peak decreased during illumination, indicating degradation of 2D layer. GIXRD patterns of ITO/SnO_2/3D/2D under (d, h) top illumination and (e, i) bottom illumination. For both glass/3D/2D and ITO/SnO_2/3D/2D, the top illumination leads to faster degradation than the bottom illumination. Schematic representations of sample architectures and illumination directions are attached to the top of each column of GIXRD patterns.

We used GIXRD to probe the depth-resolved composition change of the 2D/3D stacks during illumination aging. The penetration depths of grazing X-ray for perovskite were estimated to be ~8 and 500 nm for the incident angles of 0.2° and 3°, respectively.[34] The thickness of the 2D/3D

perovskite stacks was measured to be ~400 nm by the cross-sectional SEM (Figure S7). Thus, the diffraction data from the low incident angle of 0.2° contains structural information close to the 2D/3D interface. The X-ray diffraction data from the higher incident angle of 3° includes structural information of the bulk of 2D/3D stacks. (Figure 1a) When ω=3°, The GIXRD patterns show characteristic peaks of the 3D $MAPbI_3$ at 14°, 28°, and 31.8°, corresponding to (110), (220) and (310) planes, respectively (Figure S8a).[35] For the 2D phase, the GIXRD patterns show characteristic peaks at 5.4°, 10.8° and 16.2° corresponding to (020), (040) and (060) planes of n=1 PEA_2PbI_4, respectively.[36] A peak at 4° corresponding to the (020) planes of n=2 $PEA_2MAPb_2I_7$ is also observed, implying that the 2D layer is a mixture composed predominantly of n=1 with a small amount of n=2 2D perovskite (Figure S8a). We note that for ITO/PTAA/CuI/3D/2D, the content of n=2 2D phase increased compared to other configurations. When ω=0.2°, the GIXRD patterns show a diffraction peak at 5.4°, corresponding to the (020) plane of n=1 PEA_2PbI_4 (Figure S8b). The peaks related to 3D $MAPbI_3$ can barely be seen. Given that the penetration depth of the incident X-ray is estimated to be ~8 nm, the diffraction data mainly captures the crystal information at the surface of the 2D layer, which allows us to disentangle the ion migration and resultant crystallinity changes close to the 2D/3D interface and in the bulk.

We illuminated the encapsulated 2D/3D stacks on different HTLs and on SnO_2 with white LED light (100 mW cm^{-2}) in ambient air. The samples were illuminated either from the top (2D layer side) or from the bottom (3D layer side) to investigate how illumination direction affects the ion migration at the interface. GIXRD data was obtained on these 2D/3D stacks after 10, 24, and 45 h of illumination. The diffraction data with ω=3°, after illumination, shows that the intensity of the (020) peak of the 2D phase decreased, which indicates the degradation of the 2D

layer, irrespective of the illumination direction (Figures 1 and 2). We used the area of the (020) peak to quantify the degradation.[37] Figure 3a and 3b summarize the trend of the (020) peak area with top and bottom illumination, respectively. When the glass/3D/2D stack was illuminated from the top, the (020) peak was at 78.1% of the pristine peak area after 10 h, 60.5% after 24 h and 46.4% after 45 h. The 2D/3D stacks on the SnO_2 showed faster degradation rate as the (020) peak area of ITO/SnO_2/3D/2D stack was 47.6% of the pristine peak after 10 h, 23.2% after 24 h and 8.9% after 45 h. The degradation of the 2D/3D stacks on the HTL were slower than those on glass and on ITO/SnO_2. Specifically, ITO/3D/2D samples exhibited similar stability as ITO/PTAA/CuI/3D/2D. The degradation of ITO/3D/2D and ITO/PTAA/CuI/3D/2D samples were slower than ITO/PTAA/3D/2D. When we illuminated the 2D/3D stacks from the bottom, the trend in the changes in (020) peak of the 2D layer was ITO≈ITO/PTAA/CuI>ITO/PTAA>glass>ITO/SnO_2 (from stable to unstable).

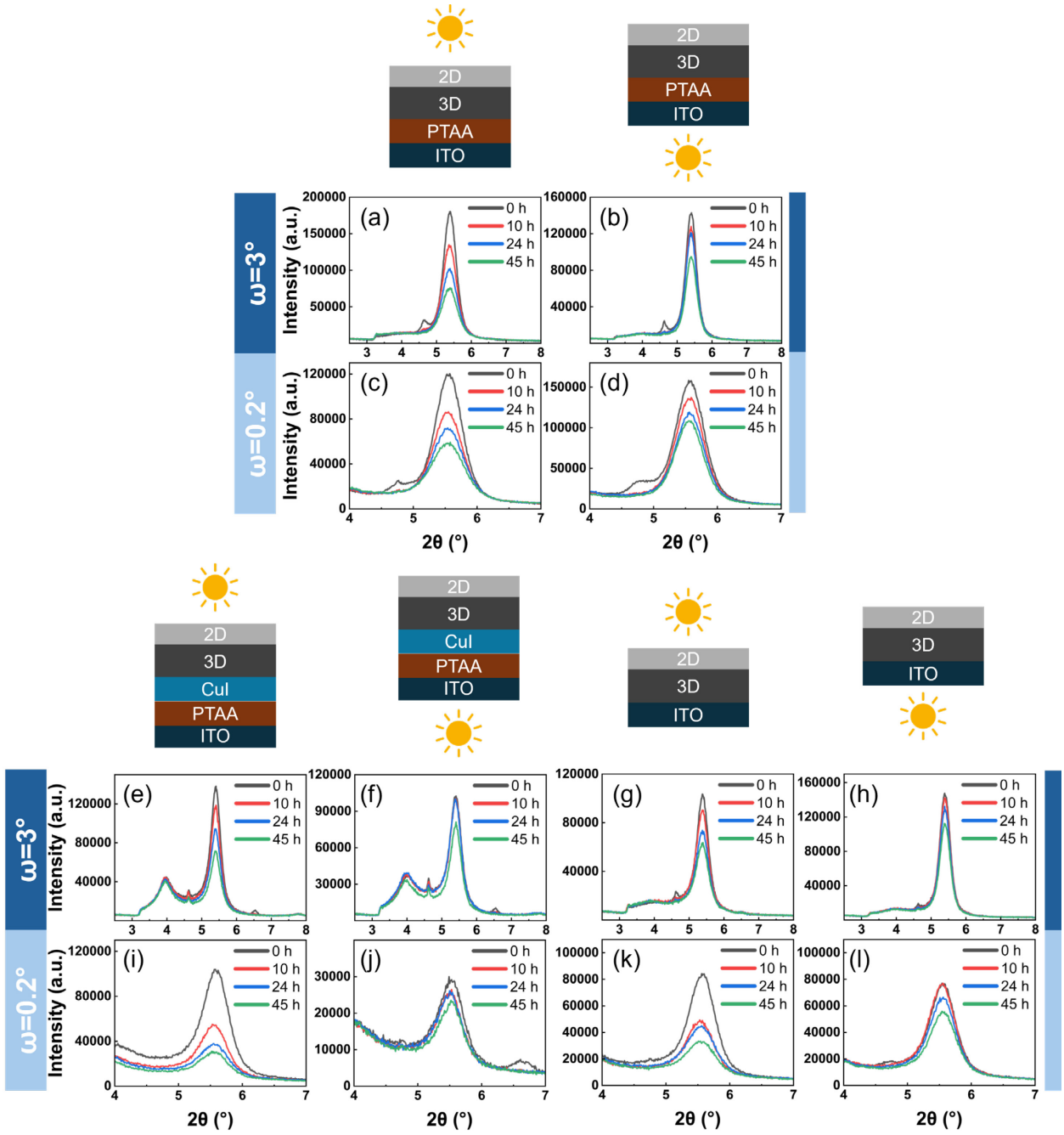

Figure 2. GIXRD patterns of (a, b, c, d) ITO/PTAA/3D/2D, (e, f, i, j) ITO/PTAA/CuI/3D/2D, and (g, h, k, l) ITO/3D/2D under either top or bottom illumination. The intensities of the (020) peak decreased during illumination, indicating degradation of the 2D layer. The surface and bulk of the

2D/3D stacks under bottom illumination are more stable than the 2D/3D stacks under top illumination.

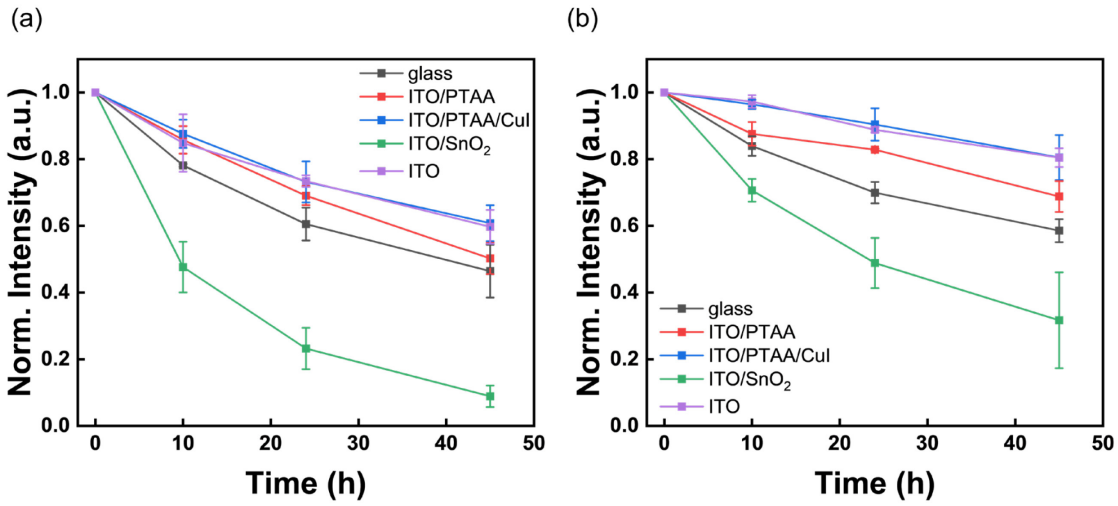

Figure 3. Summary of the evolution of the (020) peak area of 2D/3D stacks under (a) top and (b) bottom illumination. For both top and bottom illumination, 2D/3D stacks on HTL and ITO show better stability than glass/3D/2D. 2D/3D stacks on ETL exhibit the worst stability, as their (020) peak area decreased significantly faster than other samples.

Although EDS indicated the absence of K^+ and Cu^+ ions at the 2D/3D interface, we wanted to ascertain any impact of free ions in solution that may impact the stability. It is known that Cu^+ from PTAA/CuI and K^+ from the SnO_2 from Alfa Aesar (denoted as SnO_2-K) can affect the stability the 3D perovskite.[28,33,38–40] Therefore, we fabricated two samples, one with added 1% CuI and the other with 1% KI as additive in the $MAPbI_3$ precursor solution and subjected them to same illumination conditions. In the GIXRD measurements, both glass/$MAPbI_3$-CuI and glass/$MAPbI_3$-KI samples exhibited slightly better stability compared to glass/$MAPbI_3$, which are consistent with the passivation effects of Cu^+ and K^+, respectively (Figure S9a and b). Additionally, we fabricated SnO_2 ETL with no K^+ impurities following the methods reported by

Ke et al.[41] We deposited the SnO_2 layer by spin-coating a $SnCl_4 \cdot 2H_2O$ solution followed by thermal annealing in air at 180 °C for 1 hour, resulting in the SnO_2 ETL. (denoted as SnO_2-no-K). This method produced nanocrystalline SnO_2 films with no K^+ impurities. The 2D layer in the 2D/3D stacks on SnO_2-no-K exhibited reduced stability to those on SnO_2-K, which could be also attributed to the passivation effect of K^+. (Figure S9c) Overall, both added Cu^+ and K^+ ions appear to have a passivation effect that helps mitigate ion migration, thereby enhancing the stability of the 2D/3D interface. These results are also consistent with our conclusions from the EDS results that Cu^+ and K^+ do not get incorporated at the 2D/3D interface.

During the illumination aging, the 2D/3D stacks were also subjected to heating by the LED light source, which is a scenario commonly encountered in real-world conditions. It has been reported that thermal stress, as well as the combination of thermal stress and illumination, can accelerate the degradation of the 2D/3D interface.[5,16,17] In our illumination experiments, the ambient temperature reached approximately 40°C due to the light source. To isolate the effects of thermal stress, we conducted stability tests on glass/3D/2D samples in the dark at 40°C. The (020) peak of the 2D perovskite remained stable during 45 hours of thermal aging, suggesting minimal degradation under thermal stress alone. (Figure S9d) These findings indicate that the degradation of the 2D/3D interface under illumination is likely driven by the effects of light exposure or the combined influence of both thermal and light stress, rather than by thermal stress alone.

When we compared the stability of the 2D layer in the 2D/3D stacks with the same configuration between the top and bottom illumination, we found that the 2D layers undergoing bottom illumination are more stable than those undergoing top illumination (Figure S10). We employed UV-visible absorbance spectroscopy (UV-vis) to characterize the light absorption by

the 3D layer during bottom illumination. As shown in Figure S11a, all 3D samples exhibited a percent transmittance of approximately 0.1% at 518 nm, which corresponds to the absorption peak of PEA_2PbI_4 (Figure S11b). When the 2D/3D stacks are illuminated from the bottom, the 3D layer absorbs the light and the photogenerated carriers are generated closer to the bottom and away from the 2D/3D interface. We therefore conclude that reducing the charge carrier generation in the 2D layer or in the vicinity of the 2D/3D interface can improve the stability of the 2D/3D interface.

We then changed the incident angle of X-rays to 0.2° to monitor the illumination-induced changes at the surface of the 2D/3D stacks during illumination. For top or bottom illumination, the 2D (020) peak intensities decreased, indicating the degradation of the 2D surface. For 2D/3D stacks with the same configuration, the 2D surface degraded faster with top illumination than those with bottom illumination. (Figure 1 and 2). We note that the interaction volume of the X-ray of ω=0.2° with the sample is small because the estimated penetration depth is only 8 nm. It is a surface-sensitive measurement as the surface roughness and inhomogeneity might affect the interaction volume and the diffraction peak intensity. Thus, we only used the diffraction data of ω=0.2° for qualitatively probing stability. To disentangle the (020) peak intensity changes at the surface and in bulk, we calculated the changes in the normalized surface/bulk peak area ratio (see calculation details in Figure S12) during illumination.[17] The changes of diffraction intensity ratios of all 2D/3D stacks after 45 h of top illumination remained within ~20% compared to the pristine samples. (Figure S12a) For bottom illumination, the changes of diffraction intensity ratios of most 2D/3D stacks remained within ~20% compared to the pristine samples except for glass/3D/2D, which decreased to 40% of the pristine sample (Figure S12b). These results qualitatively suggest that for top illumination, the surface of 2D layers degrades approximately

as fast as the bulk for all samples. For bottom illumination, the surface of glass/3D/2D degrades faster than the bulk while the surface of ITO/3D/2D, ITO/PTAA/3D/2D, ITO/PTAA/CuI/3D/2D degrade as fast as the bulk.

We then examined the changes in the (110) peak of 3D perovskite during illumination aging. Unlike the (020) peak of 2D perovskite, the (110) peaks of 3D perovskite exhibit fluctuations but a drastic decrease in peak area is not observed (Figure S13). It suggests that changes in the crystallinity of the 3D layer are minimal. The fluctuations in peak intensity can be attributed to the complex dynamic ion migration process at the interface during illumination. Light soaking has also been reported to be able to induce the passivation of defects, which can improve crystallinity. At the same time, the cation exchange at the interface results in the incorporation of PEA^+ cation and loss of MA^+ in the 3D perovskite.[5] The stability of the 3D layer is also observed in the previous investigation of the 2D/3D stack under heat stress, suggesting that the 3D layer is not sensitive to the cation composition change.[35] Overall, the 3D layers in the 2D/3D stacks do not show severe degradation during illumination.

To characterize the photogenerated charge carrier extraction, we performed steady-state photoluminescence spectroscopy (PL) on the 2D/3D stacks. The samples were excited either from the top or bottom. For top excitation (Figure 4a), all 2D/3D stacks show a strong emission peak at 522 nm, corresponding to the n=1 2D PEA_2PbI_4 phase.[42] A weak emission peak at 560 nm indicates the existence of a small amount of n=2 2D $PEA_2MAPb_2I_7$ phase.[43] This is consistent with the GIXRD result that the majority of the 2D layer is n=1 PEA_2PbI_4 with a small amount of n=2 $PEA_2MAPb_2I_7$. The emission peak at 770 nm corresponds to the 3D $MAPbI_3$ phase.[44] For bottom excitation (Figure 4b), the PL spectra of the 2D/3D stacks show a peak at 770 nm of the 3D phase and a weak peak at 522 nm of the n=1 2D phase. We noticed that the 2D

PL peak intensities were significantly weaker when the samples were excited from the bottom than those on top, which could be attributed to the strong light absorption capability of the 3D layer. It also suggests that the charge carrier generation profiles are different between top and bottom excitation conditions. The photogenerated exciton density in the 2D layer is higher for top illumination.

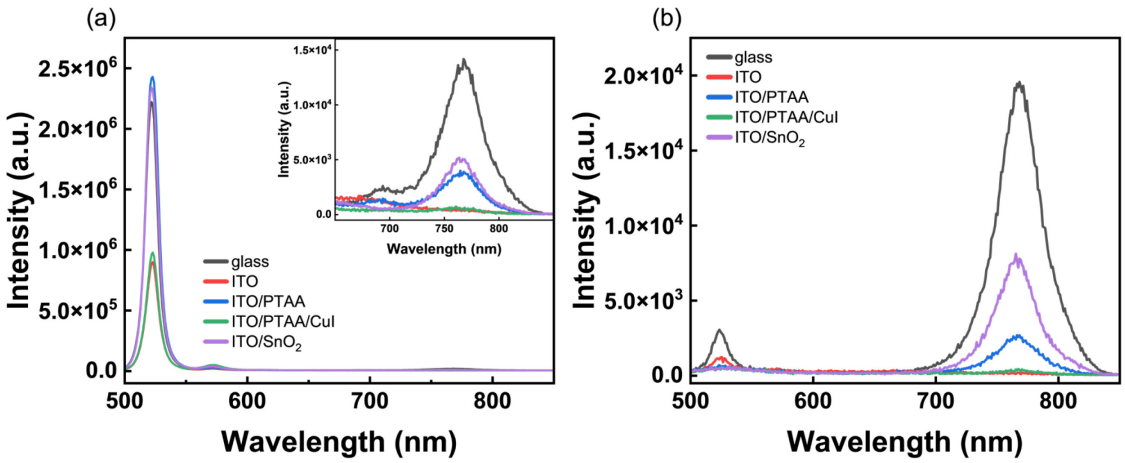

Figure 4. Steady-state photoluminescence spectroscopy of 2D/3D stacks. (a) The excitation is from the top (2D layer side). The peaks at 522 nm and 560 nm correspond to the n=1 and n=2 2D phase, respectively. The inset shows the magnified peaks at 770 nm, corresponding to the 3D phase. (b) The excitation is from the bottom (3D layer side). The peaks at 522 nm and 770 nm correspond to the n=1 2D and 3D phase, respectively. In this case, the 522 nm 2D peaks are weaker than those with top excitation, suggesting lower charge carrier generation and recombination rate in the 2D layer with bottom excitation.

2D/3D stacks deposited on ITO/PTAA, ITO/PTAA/CuI, ITO/SnO_2 and bare ITO show quenched PL intensity of the 770 nm peak compared to that on glass, which could be indicative of charge extraction or increased non-radiative recombination. We summarize the 770 nm peak

intensity of glass/3D/2D, ITO/PTAA/3D/2D and ITO/PTAA/CuI/3D/2D in Table S3 to investigate the hole extraction efficiency by the HTL and ITO. ITO/PTAA/CuI/3D/2D and ITO/3D/2D display the lowest PL intensity of the 770 nm peak, due to better hole extraction than PTAA. Interestingly, the intensity of the 522 nm peaks of the 2D/3D stacks deposited on ITO and ITO/PTAA/CuI are lower than those on glass, ITO/PTAA and ITO/SnO_2, with top excitation. This implies that the efficient hole extraction from the 3D layer could also impact the photogenerated charge carrier densities in the 2D layer above it, which could be attributed to the charge transfer between the 2D and 3D layers.

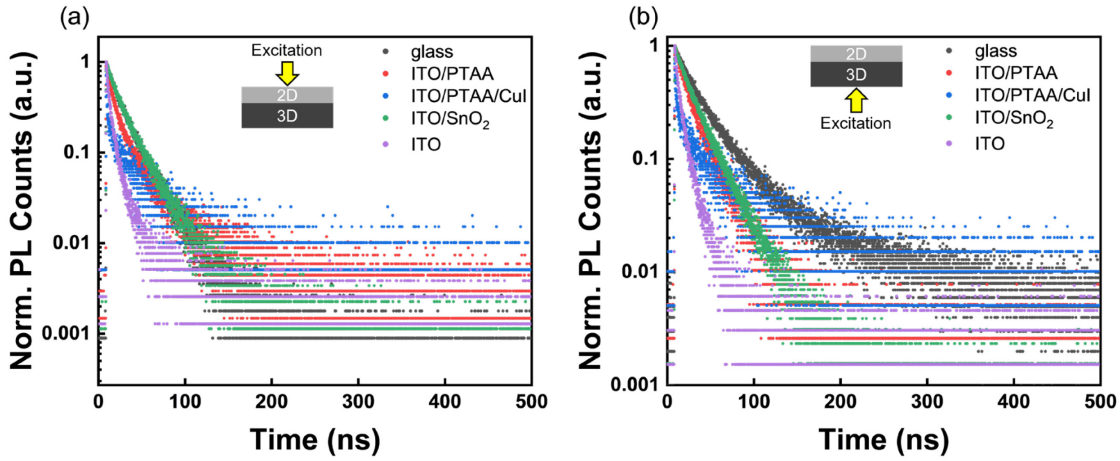

Figure 5. PL decay transients in the 500 ns range of 2D/3D stacks with (a) top excitation and (b) bottom excitation. For both top and bottom excitation, 2D/3D stacks on HTL, ETL and ITO exhibit faster PL decay than glass/3D/2D. For the HTL used, PTAA/CuI shows a distinctive 2-stage decay profile due to the faster hole extraction. The difference in hole extraction capabilities of PTAA/CuI and PTAA allows us to correlate the hole extraction rate to the stability of the 2D/3D stacks.

Table 1. Summary of lifetime constants of 2D/3D stacks

Sample	Excitation direction	τ_1 (ns)	τ_2 (ns)
glass/3D/2D	Top	12.16±0.61	27.94±1.40
glass/3D/2D	Bottom	27.99±1.40	119.72±5.99
ITO/PTAA/3D/2D	Top	9.07±0.45	40.81±2.04
ITO/PTAA/3D/2D	Bottom	9.66±0.48	25.99±1.30
ITO/PTAA/CuI/3D/2D	Top	0.58±0.03	28.57±1.43
ITO/PTAA/CuI/3D/2D	Bottom	3.19±0.16	48.53±2.43
ITO/SnO_2/3D/2D	Top	10.75±0.54	27.67±1.38
ITO/SnO_2/3D/2D	Bottom	14.15±0.71	28.97±1.45
ITO/3D/2D	Top	3.94±0.20	18.72±0.94
ITO/3D/2D	Bottom	3.63±0.18	14.16±0.71

To further understand the charge carrier dynamics in the 2D/3D stacks, we performed time-resolved photoluminescence spectroscopy (TRPL). The samples are excited by a 405 nm laser and the PL decay is recorded at 770 nm. Figure 5a and 5b show the PL transients with top and bottom excitation, respectively. The decay of TRPL is governed by bimolecular radiative recombination, monomolecular trap-assisted recombination, and charge transfer to the underlying charge transport layers.[45–49] The PL transients of 2D/3D stacks on HTL, ETL and ITO display faster decay than on bare glass, resulting from the charge extraction. The PL transients were fitted to a bi-exponential decay model to extract the lifetime constants. The lifetime constants, τ_1 and τ_2, are summarized in Table 1. The fast lifetime, τ_1, is attributed to charge extraction by the HTL, ETL or ITO while the slower lifetime, τ_2, is attributed to bimolecular bulk or interface recombination.[46,47] The τ_1 of ITO/PTAA/CuI/3D/2D (top excitation: 0.58 ns; bottom excitation: 3.19 ns) and ITO/3D/2D(top excitation: 3.94 ns; bottom excitation: 3.63 ns) are smaller than the τ_1 of ITO/PTAA/3D/2D(top excitation: 9.07 ns; bottom

excitation: 9.66 ns). The smaller τ_1 indicates faster charge transfer from the 3D layer to PTAA/CuI or ITO than to PTAA.

We note that relying solely on PL quenching as evidence of efficient charge extraction could be misleading. The observed shorter PL lifetimes and reduced peak intensities should be interpreted with caution, as they may also indicate increased non-radiative recombination rather than solely efficient charge extraction. To further verify the hole extraction capabilities of the PTAA/CuI bilayer compared to PTAA alone, we fabricated full photovoltaic devices with structures of ITO/PTAA/3D/2D/PCBM/C_{60}-N/Ag and ITO/PTAA/CuI/3D/2D/PCBM/C_{60}-N/Ag. The photovoltaic performances are summarized in Table S4. The devices with PTAA/CuI as the HTL exhibited superior photovoltaic parameters, including higher V_{oc} (1.042 V vs. 1.024 V), J_{sc} (25.36 mA cm^{-2} vs. 23.93 mA cm^{-2}), FF (72.57 vs. 70.88), and PCE (19.18% vs. 17.37%) compared to those with PTAA alone. The higher V_{oc} and J_{sc} of the PTAA/CuI devices provide evidence of more efficient hole extraction and possibly better passivation at the HTL/3D interface. The improvement in device performance further supports the faster PL decay observed in the TRPL measurements, indicating better charge transfer dynamics with the PTAA/CuI bilayer.

With the studies of the stability of 2D/3D stacks by GIXRD and studies of the charge carrier extraction by PL and TRPL, we are now able to correlate the impact of the photogenerated charge carriers on the stability of the 2D/3D interface. For either top or bottom illumination, 2D/3D stacks on HTL and ITO exhibit slower degradation of the 2D layer than 2D/3D stacks on glass while 2D/3D stacks on ETL exhibit faster degradation than 2D/3D stacks on glass. These samples represent 4 types of charge carrier conditions in the 3D layer: (1) extracting holes (ITO/PTAA, ITO/PTAA/CuI), (2) no charge carrier extraction (glass), (3) extracting electrons

(ITO/SnO_2), and (4) non-selective charge carrier extraction (ITO). Thus, we hypothesize that the accumulation of photogenerated holes in the 3D layer results in faster illumination-induced degradation of the 2D perovskite layer. Among the HTL used, PTAA/CuI showed slower degradation of the 2D layer than PTAA. Samples on ITO show a degradation rate compared to PTAA/CuI. The PL and TRPL studies indicate that PTAA/CuI and ITO are more efficient in hole extraction than PTAA, which is consistent with our previous work.[38] Thus, we speculate that the more efficient hole extraction from the 3D perovskite increases the stability of the 2D layer under illumination.

When we compare the stability of the 2D layer of the 2D/3D stacks with the same configuration but different incident direction of illumination, we find that illuminating samples far from the 2D/3D interface (bottom) results in a slower degradation than illuminating samples closer to the 2D/3D interface (top). The PL study shows that the directions of excitation light significantly affect the emission peak intensity of the 2D perovskite. The 522 nm peak intensity is significantly stronger with top excitation light than with bottom excitation light. It also suggests that the exciton density in the 2D perovskite is higher when the 2D/3D stacks are illuminated from the 2D layer side because the 3D perovskite strongly absorbs the light if the 2D/3D stacks are illuminated from the 3D layer side. Thus, we conclude that reducing the exciton density in the 2D layer can slow down the degradation.

We also find that the surface of the 2D layer degrades as fast as the bulk for top illumination. For bottom illumination, the surface of glass/3D/2D degrades faster than the bulk while the surface of 2D/3D stacks on HTL or ITO degrades as fast as the bulk. If the degradation of the 2D layer is solely due to the cation exchange at the interface, one would expect that the top surface of the 2D layer (away from the interface) degrades slower than the part closer to the interface.

However, our GIXRD data with ω=0.2° suggests that the loss of crystallinity at the surface of the 2D layer is not slower than the bulk. A recent study by Perini et al. used GIWAXS and XPS to study the thermal-induced reconstruction at the surface and in the bulk of 2D/3D perovskite.[17] They found that FA^+ diffusion-induced phase transformation and the loss of crystallinity together contributed to the loss of orientation of the 2D layer upon thermal annealing. Similarly, we posit that photogenerated charge carriers not only aggravate the cation migration at the interface but also result in loss of crystallinity in the whole 2D layer. It is necessary to arrest the ion migration in the 2D layer and also the 2D/3D interface to achieve long-term stability.

For the stability of the 3D layer under illumination, we did not observe severe degradation as the area of (110) peak of 3D perovskite did not show drastic degradation. A recent study by Mathew and Kamat probed the thermal-driven cation migration at the interface of physically paired 2D and 3D perovskite films.[35] In their findings, the migration of MA^+ toward the 2D layer transforms the n=1 2D phase into phases with higher n-values. The 2D phase is sensitive to the exchange of cations because a small change in the ratio of small/large A-site cations can change the phase of 2D. On the other hand, a combination of XRD and PL studies showed that the 3D phase is less sensitive to cation composition changes. Based on their observations and our GIXRD studies, we therefore conclude that the illumination-induced cation migration will not lead to severe degradation in the 3D layer. This is consistent with many studies in which the 2D layer serves as a protective capping layer to improve the stability of PSCs.[1,7,9,50,51]

Based on the discussion above, we propose the correlation between the photogenerated charge carriers and the degradation of the 2D/3D interface. The charge carriers in both the 2D and 3D layers need to be considered for the cation migration. When illuminated from the top, the high exciton density in the 2D perovskite reduces the barriers for ion migration in the 2D layer. The

aggravated cation exchange at the 2D/3D interface and aggravated ion migration in the 2D layer together contribute to the loss of crystallinity of the 2D layer. In terms of the photogenerated charge carriers in the 3D layer, extracting holes efficiently from the 3D layer suppresses the cation activity in the 3D layer and thus reduces the cation exchange at the 2D/3D interface. To achieve stable 2D/3D interface, the holes in the 3D layer should be efficiently extracted and the exciton density in the 2D layer should be reduced.

CONCLUSIONS

In this work, we investigated the impact of photogenerated charge carriers on the stability of the 2D/3D interface. We fabricated 2D/3D perovskite stacks on glass, ITO, ITO/PTAA, ITO/PTAA/CuI and ITO/SnO_2 and used GIXRD to monitor their stability under illumination. GIXRD studies show that the intensity of the (020) peak of the 2D perovskite decreases during illumination aging, indicating the degradation of the 2D layer. The stability of the 2D layer follows the trend of ITO/PTAA/CuI≈ITO>ITO/PTAA>glass>ITO/SnO_2 (from stable to unstable). This trend reveals that the accumulation of photogenerated holes, instead of electrons, is the cause of ion migration at the 2D/3D interface. Illuminating the 2D/3D stacks from the 2D side results in faster degradation than illuminating the 2D/3D stacks from the 3D side. The 3D layer undergoes dynamic ion migration but does not exhibit severe degradation. After acquiring the stability of the 2D/3D stacks under illumination, we use PL and TRPL to investigate the charge carrier extraction in these 2D/3D stacks. PL and TRPL on these 2D/3D stacks show that ITO and ITO/PTAA/CuI exhibit more efficient hole extraction than PTAA. For different incident light directions, 2D/3D stacks with top illumination show a stronger emission peak at 522 nm than with bottom illumination, suggesting that the top illumination induces a higher exciton density in the 2D layer. Thus, the faster degradation of the 2D layer with top illumination is

associated with the high exciton density. Based on these observations, we propose that the charge carriers in both the 2D and 3D layers have an impact on the stability of the 2D/3D interface. The high photogenerated exciton density in the 2D layer and the accumulation of holes in the 3D layers accelerate the MA^+ migration from the 3D to 2D layer, leading to faster degradation of the 2D layer. To achieve a stable 2D/3D interface, hole accumulation should be avoided in the 3D layer and the exciton density in the 2D layer should be reduced.

Supporting Information

SEM images of 3D films and 2D/3D stack, cross-sectional SEM image of 2D/3D stack, AFM images of 3D films and 2D/3D stacks, EDS results of distribution of Cu and K in the 3D films, GIXRD patterns of 2D/3D stacks, comparison of (020) peak area with top and bottom illumination, and surface/bulk peak area ratio, photovoltaic performances of PSCs with PTAA and PTAA/CuI.

Data Availability Statement

The data underlying this study are openly available in Scholarworks@UMassAmherst at DOI [Will be provided after acceptance]

AUTHOR INFORMATION

Corresponding Author

D. Venkataraman – Department of Chemistry, University of Massachusetts Amherst, Amherst, MA 01003, United States; orcid.org/0000-0003-2906-0579; Email: dv@umass.edu

Authors

Zhaojie Zhang - Department of Chemistry, University of Massachusetts Amherst, Amherst, MA 01003, United States; orcid.org/0000-0001-9259-4720

Miu Tsuji - Department of Chemistry, University of Connecticut, Storrs, CT 06269, United States; orcid.org/0009-0001-7634-9343

Xin Hu - Department of Polymer Science and Engineering, University of Massachusetts Amherst, Amherst, MA 01003, United States; orcid.org/0000-0001-9355-6072

Tomoyasu Mani - Department of Chemistry, University of Connecticut, Storrs, CT 06269, United States; orcid.org/0000-0002-4125-5195

Author Contributions

DV and ZZ designed the studies. DV directed and supervised the research. ZZ prepared the perovskite films, performed GIXRD and PL measurements, and interpreted the GIXRD and PL data. MT and TM performed the TRPL measurements and interpreted the TRPL data. XH performed the cross-sectional SEM.

Notes

The authors declare no competing financial interest.

ACKNOWLEDGMENT

We dedicate this work to the memory of Prof. Francis J. DiSalvo. DV and ZZ acknowledge support from US National Science Foundation (NSF) DMR 2101127. We also thank PPG Foundation for a graduate fellowship to ZZ. Powder X-ray diffractometer, which was used for our

studies, was purchased through NSF Major Research Instrumentation grant CHE-1726578. TM acknowledges NSF under Grant CHE-2144787, an NSF CAREER Award. We thank Dr. Alexander Ribbe for acquiring the EDS data.

REFERENCES

(1) Wen, J.; Zhao, Y.; Wu, P.; Liu, Y.; Zheng, X.; Lin, R.; Wan, S.; Li, K.; Luo, H.; Tian, Y.; Li, L.; Tan, H. Heterojunction Formed via 3D-to-2D Perovskite Conversion for Photostable Wide-Bandgap Perovskite Solar Cells. *Nat. Commun.* **2023**, *14* (1), 7118. https://doi.org/10.1038/s41467-023-43016-5.

(2) Metcalf, I.; Sidhik, S.; Zhang, H.; Agrawal, A.; Persaud, J.; Hou, J.; Even, J.; Mohite, A. D. Synergy of 3D and 2D Perovskites for Durable, Efficient Solar Cells and Beyond. *Chem. Rev.* **2023**, *123* (15), 9565–9652. https://doi.org/10.1021/acs.chemrev.3c00214.

(3) Chen, P.; He, D.; Huang, X.; Zhang, C.; Wang, L. Bilayer 2D-3D Perovskite Heterostructures for Efficient and Stable Solar Cells. *ACS Nano* **2023**, *18* (1), 67–88. https://doi.org/10.1021/acsnano.3c09176.

(4) Luo, L.; Zeng, H.; Wang, Z.; Li, M.; You, S.; Chen, B.; Maxwell, A.; An, Q.; Cui, L.; Luo, D.; Hu, J.; Li, S.; Cai, X.; Li, W.; Li, L.; Guo, R.; Huang, R.; Liang, W.; Lu, Z.-H.; Mai, L.; Rong, Y.; Sargent, E. H.; Li, X. Stabilization of 3D/2D Perovskite Heterostructures via Inhibition of Ion Diffusion by Cross-Linked Polymers for Solar Cells with Improved Performance. *Nat. Energy* **2023**, *8* (3), 294–303. https://doi.org/10.1038/s41560-023-01205-y.

(5) Fiorentino, F.; Albaqami, M. D.; Poli, I.; Petrozza, A. Thermal- and Light-Induced Evolution of the 2D/3D Interface in Lead-Halide Perovskite Films. *ACS Appl. Mater. Interfaces* **2022**, *14* (30), 34180–34188. https://doi.org/10.1021/acsami.1c09695.

(6) Sidhik, S.; Wang, Y.; Li, W.; Zhang, H.; Zhong, X.; Agrawal, A.; Hadar, I.; Spanopoulos, I.; Mishra, A.; Traoré, B.; Samani, M. H. K.; Katan, C.; Marciel, A. B.; Blancon, J.-C.; Even, J.; Kahn, A.; Kanatzidis, M. G.; Mohite, A. D. High-Phase Purity Two-Dimensional Perovskites with 17.3% Efficiency Enabled by Interface Engineering of Hole Transport Layer. *Cell Rep. Phys. Sci.* **2021**, *2* (10), 100601. https://doi.org/10.1016/j.xcrp.2021.100601.

(7) Wu, G.; Liang, R.; Ge, M.; Sun, G.; Zhang, Y.; Xing, G. Surface Passivation Using 2D Perovskites toward Efficient and Stable Perovskite Solar Cells. *Adv. Mater.* **2022**, *34* (8), 2105635. https://doi.org/10.1002/adma.202105635.

(8) Cho, K. T.; Grancini, G.; Lee, Y.; Oveisi, E.; Ryu, J.; Almora, O.; Tschumi, M.; Schouwink, P. A.; Seo, G.; Heo, S.; Park, J.; Jang, J.; Paek, S.; Garcia-Belmonte, G.; Nazeeruddin, M. K. Selective Growth of Layered Perovskites for Stable and Efficient Photovoltaics. *Energy Environ. Sci.* **2018**, *11* (4), 952–959. https://doi.org/10.1039/C7EE03513F.

(9) Azmi, R.; Ugur, E.; Seitkhan, A.; Aljamaan, F.; Subbiah, A. S.; Liu, J.; Harrison, G. T.; Nugraha, M. I.; Eswaran, M. K.; Babics, M.; Chen, Y.; Xu, F.; Allen, T. G.; Rehman, A. ur; Wang, C.-L.; Anthopoulos, T. D.; Schwingenschlögl, U.; De Bastiani, M.; Aydin, E.; De Wolf, S. Damp Heat–Stable Perovskite Solar Cells with Tailored-Dimensionality 2D/3D Heterojunctions. *Science* **2022**, *376* (6588), 73–77. https://doi.org/10.1126/science.abm5784.

(10) Azmi, R.; Utomo, D. S.; Vishal, B.; Zhumagali, S.; Dally, P.; Risqi, A. M.; Prasetio, A.; Ugur, E.; Cao, F.; Imran, I. F.; Said, A. A.; Pininti, A. R.; Subbiah, A. S.; Aydin, E.; Xiao, C.;

Seok, S. I.; De Wolf, S. Double-Side 2D/3D Heterojunctions for Inverted Perovskite Solar Cells. *Nature* **2024**, *628* (8006), 93–98. https://doi.org/10.1038/s41586-024-07189-3.

(11) Grancini, G.; Roldán-Carmona, C.; Zimmermann, I.; Mosconi, E.; Lee, X.; Martineau, D.; Narbey, S.; Oswald, F.; De Angelis, F.; Graetzel, M.; Nazeeruddin, M. K. One-Year Stable Perovskite Solar Cells by 2D/3D Interface Engineering. *Nat. Commun.* **2017**, *8* (1), 15684. https://doi.org/10.1038/ncomms15684.

(12) Kore, B. P.; Zhang, W.; Hoogendoorn, B. W.; Safdari, M.; Gardner, J. M. Moisture Tolerant Solar Cells by Encapsulating 3D Perovskite with Long-Chain Alkylammonium Cation-Based 2D Perovskite. *Commun. Mater.* **2021**, *2* (1), 1–10. https://doi.org/10.1038/s43246-021-00200-8.

(13) Chen, J.; Yang, Y.; Dong, H.; Li, J.; Zhu, X.; Xu, J.; Pan, F.; Yuan, F.; Dai, J.; Jiao, B.; Hou, X.; Jen, A. K.-Y.; Wu, Z. Highly Efficient and Stable Perovskite Solar Cells Enabled by Low-Dimensional Perovskitoids. *Sci. Adv.* **2022**, *8* (4), eabk2722. https://doi.org/10.1126/sciadv.abk2722.

(14) Szabó, G.; Kamat, P. V. How Cation Migration across a 2D/3D Interface Dictates Perovskite Solar Cell Efficiency. *ACS Energy Lett.* **2023**, *9* (1), 193–200. https://doi.org/10.1021/acsenergylett.3c02503.

(15) Sutanto, A. A.; Szostak, R.; Drigo, N.; Queloz, V. I. E.; Marchezi, P. E.; Germino, J. C.; Tolentino, H. C. N.; Nazeeruddin, M. K.; Nogueira, A. F.; Grancini, G. In Situ Analysis Reveals the Role of 2D Perovskite in Preventing Thermal-Induced Degradation in 2D/3D Perovskite Interfaces. *Nano Lett.* **2020**, *20* (5), 3992–3998. https://doi.org/10.1021/acs.nanolett.0c01271.

(16) Sutanto, A. A.; Drigo, N.; Queloz, V. I. E.; Garcia-Benito, I.; Kirmani, A. R.; Richter, L. J.; Schouwink, P. A.; Cho, K. T.; Paek, S.; Nazeeruddin, M. K.; Grancini, G. Dynamical Evolution of the 2D/3D Interface: A Hidden Driver behind Perovskite Solar Cell Instability. *J. Mater. Chem. A* **2020**, *8* (5), 2343–2348. https://doi.org/10.1039/C9TA12489F.

(17) Perini, C. A. R.; Rojas-Gatjens, E.; Ravello, M.; Castro-Mendez, A.-F.; Hidalgo, J.; An, Y.; Kim, S.; Lai, B.; Li, R.; Silva-Acuña, C.; Correa-Baena, J.-P. Interface Reconstruction from Ruddlesden–Popper Structures Impacts Stability in Lead Halide Perovskite Solar Cells. *Adv. Mater.* **2022**, *34* (51), 2204726. https://doi.org/10.1002/adma.202204726.

(18) Park, S. M.; Wei, M.; Xu, J.; Atapattu, H. R.; Eickemeyer, F. T.; Darabi, K.; Grater, L.; Yang, Y.; Liu, C.; Teale, S.; Chen, B.; Chen, H.; Wang, T.; Zeng, L.; Maxwell, A.; Wang, Z.; Rao, K. R.; Cai, Z.; Zakeeruddin, S. M.; Pham, J. T.; Risko, C. M.; Amassian, A.; Kanatzidis, M. G.; Graham, K. R.; Grätzel, M.; Sargent, E. H. Engineering Ligand Reactivity Enables High-Temperature Operation of Stable Perovskite Solar Cells. *Science* **2023**, *381* (6654), 209–215. https://doi.org/10.1126/science.adi4107.

(19) Domanski, K.; Alharbi, E. A.; Hagfeldt, A.; Grätzel, M.; Tress, W. Systematic Investigation of the Impact of Operation Conditions on the Degradation Behaviour of Perovskite Solar Cells. *Nat. Energy* **2018**, *3* (1), 61–67. https://doi.org/10.1038/s41560-017-0060-5.

(20) Slotcavage, D. J.; Karunadasa, H. I.; McGehee, M. D. Light-Induced Phase Segregation in Halide-Perovskite Absorbers. *Acs Energy Lett.* **2016**, *1* (6), 1199–1205. https://doi.org/10.1021/acsenergylett.6b00495.

(21) Mathew, P.; Cho, J.; Kamat, P. V. Ramifications of Ion Migration in 2D Lead Halide Perovskites. *ACS Energy Lett.* **2024**, *9* (3), 1103–1114. https://doi.org/10.1021/acsenergylett.4c00093.

(22) Lin, Y.; Chen, B.; Fang, Y.; Zhao, J.; Bao, C.; Yu, Z.; Deng, Y.; Rudd, P. N.; Yan, Y.; Yuan, Y.; Huang, J. Excess Charge-Carrier Induced Instability of Hybrid Perovskites. *Nat. Commun.* **2018**, *9* (1), 4981. https://doi.org/10.1038/s41467-018-07438-w.

(23) DuBose, J. T.; Kamat, P. V. TiO2-Assisted Halide Ion Segregation in Mixed Halide Perovskite Films. *J. Am. Chem. Soc.* **2020**, *142* (11), 5362–5370. https://doi.org/10.1021/jacs.0c00434.

(24) Tan, S.; Huang, T.; Yavuz, I.; Wang, R.; Yoon, T. W.; Xu, M.; Xing, Q.; Park, K.; Lee, D. K.; Chen, C. H.; Zheng, R.; Yoon, T.; Zhao, Y.; Wang, H. C.; Meng, D.; Xue, J.; Song, Y. J.; Pan, X.; Park, N. G.; Lee, J. W.; Yang, Y. Stability-Limiting Heterointerfaces of Perovskite Photovoltaics. *Nature* **2022**, *605*, 268–273. https://doi.org/10.1038/s41586-022-04604-5.

(25) Yan, X.; Fan, W.; Cheng, F.; Sun, H.; Xu, C.; Wang, L.; Kang, Z.; Zhang, Y. Ion Migration in Hybrid Perovskites: Classification, Identification, and Manipulation. *Nano Today* **2022**, *44*, 101503. https://doi.org/10.1016/j.nantod.2022.101503.

(26) Tong, C.-J.; Cai, X.; Zhu, A.-Y.; Liu, L.-M.; Prezhdo, O. V. How Hole Injection Accelerates Both Ion Migration and Nonradiative Recombination in Metal Halide Perovskites. *J. Am. Chem. Soc.* **2022**, *144* (14), 6604–6612. https://doi.org/10.1021/jacs.2c02148.

(27) DuBose, J. T.; Kamat, P. V. Hole Trapping in Halide Perovskites Induces Phase Segregation. *Acc. Mater. Res.* **2022**, *3* (7), 761–771. https://doi.org/10.1021/accountsmr.2c00076.

(28) Bu, T.; Li, J.; Zheng, F.; Chen, W.; Wen, X.; Ku, Z.; Peng, Y.; Zhong, J.; Cheng, Y.-B.; Huang, F. Universal Passivation Strategy to Slot-Die Printed SnO2 for Hysteresis-Free Efficient Flexible Perovskite Solar Module. *Nat. Commun.* **2018**, *9* (1), 4609. https://doi.org/10.1038/s41467-018-07099-9.

(29) Abdi-Jalebi, M.; Andaji-Garmaroudi, Z.; Cacovich, S.; Stavrakas, C.; Philippe, B.; Richter, J. M.; Alsari, M.; Booker, E. P.; Hutter, E. M.; Pearson, A. J.; Lilliu, S.; Savenije, T. J.; Rensmo, H.; Divitini, G.; Ducati, C.; Friend, R. H.; Stranks, S. D. Maximizing and Stabilizing Luminescence from Halide Perovskites with Potassium Passivation. *Nature* **2018**, *555* (7697), 497–501. https://doi.org/10.1038/nature25989.

(30) Yang, Y.; Wu, L.; Hao, X.; Tang, Z.; Lai, H.; Zhang, J.; Wang, W.; Feng, L. Beneficial Effects of Potassium Iodide Incorporation on Grain Boundaries and Interfaces of Perovskite Solar Cells. *RSC Adv.* **2019**, *9* (49), 28561–28568. https://doi.org/10.1039/C9RA05371A.

(31) Dagar, J.; Hirselandt, K.; Merdasa, A.; Czudek, A.; Munir, R.; Zu, F.; Koch, N.; Dittrich, T.; Unger, E. L. Alkali Salts as Interface Modifiers in N-i-p Hybrid Perovskite Solar Cells. *Sol. RRL* **2019**, *3* (9), 1900088. https://doi.org/10.1002/solr.201900088.

(32) Wang, P.; Wang, J.; Zhang, X.; Wang, H.; Cui, X.; Yuan, S.; Lu, H.; Tu, L.; Zhan, Y.; Zheng, L. Boosting the Performance of Perovskite Solar Cells through a Novel Active Passivation Method. *J. Mater. Chem. A* **2018**, *6* (32), 15853–15858. https://doi.org/10.1039/C8TA05593A.

(33) I. Alanazi, T.; S. Game, O.; A. Smith, J.; C. Kilbride, R.; Greenland, C.; Jayaprakash, R.; Georgiou, K.; J. Terrill, N.; G. Lidzey, D. Potassium Iodide Reduces the Stability of Triple-Cation Perovskite Solar Cells. *RSC Adv.* **2020**, *10* (66), 40341–40350. https://doi.org/10.1039/D0RA07107B.

(34) Chen, W.; Gan, Z.; Green, M. A.; Jia, B.; Wen, X. Revealing Dynamic Effects of Mobile Ions in Halide Perovskite Solar Cells Using Time-Resolved Microspectroscopy. *Small Methods* **2021**, *5* (1), e2000731. https://doi.org/10.1002/smtd.202000731.

(35) Mathew, P. S.; Kamat, P. V. Cation Migration in Physically Paired 2D and 3D Lead Halide Perovskite Films. *Adv. Opt. Mater.* **2023**, *12* (8), 2300957. https://doi.org/10.1002/adom.202300957.

(36) La-Placa, M.-G.; Guo, D.; Gil-Escrig, L.; Palazon, F.; Sessolo, M.; Bolink, H. J. Dual-Source Vacuum Deposition of Pure and Mixed Halide 2D Perovskites: Thin Film Characterization and Processing Guidelines. *J. Mater. Chem. C* **2020**, *8* (6), 1902–1908. https://doi.org/10.1039/C9TC06662D.

(37) Ellis, C. L. C.; Javaid, H.; Smith, E. C.; Venkataraman, D. Hybrid Perovskites with Larger Organic Cations Reveal Autocatalytic Degradation Kinetics and Increased Stability under Light. *Inorg. Chem.* **2020**, *59* (17), 12176–12186. https://doi.org/10.1021/acs.inorgchem.0c01133.

(38) Zhang, Z.; Gilchrist, R. J.; Tsuji, M.; Grimm, R. L.; Mani, T.; Venkataraman, D. Synergistic Impact of Passivation and Efficient Hole Extraction on Phase Segregation in Mixed Halide Perovskites. *Adv. Opt. Mater.* **2024**, 2401753. https://doi.org/10.1002/adom.202401753.

(39) He, R.; Wu, Y.; Li, Z.; Wang, Y.; Zhu, W.; Tong, A.; Chen, X.; Pan, W.; Sun, W.; Wu, J. Bulk and Interface Passivation through Potassium Iodide Additives Engineering Enables High-Performance and Humidity-Stable CsPbBr3 Perovskite Solar Cells. *Surf. Interfaces* **2024**, *48*, 104274. https://doi.org/10.1016/j.surfin.2024.104274.

(40) Zhang, M.; Bing, J.; Cho, Y.; Li, Y.; Zheng, J.; Lau, C. F. J.; Green, M. A.; Huang, S.; Ho-Baillie, A. W. Y. Synergistic Effect of Potassium and Iodine from Potassium Triiodide Complex Additive on Gas-Quenched Perovskite Solar Cells. *Nano Energy* **2019**, *63*, 103853. https://doi.org/10.1016/j.nanoen.2019.06.049.

(41) Ke, W.; Fang, G.; Liu, Q.; Xiong, L.; Qin, P.; Tao, H.; Wang, J.; Lei, H.; Li, B.; Wan, J.; Yang, G.; Yan, Y. Low-Temperature Solution-Processed Tin Oxide as an Alternative Electron Transporting Layer for Efficient Perovskite Solar Cells. *J. Am. Chem. Soc.* **2015**, *137* (21), 6730–6733. https://doi.org/10.1021/jacs.5b01994.

(42) Laitz, M.; Kaplan, A. E. K.; Deschamps, J.; Barotov, U.; Proppe, A. H.; García-Benito, I.; Osherov, A.; Grancini, G.; deQuilettes, D. W.; Nelson, K. A.; Bawendi, M. G.; Bulović, V. Uncovering Temperature-Dependent Exciton-Polariton Relaxation Mechanisms in Hybrid Organic-Inorganic Perovskites. *Nat. Commun.* **2023**, *14* (1), 2426. https://doi.org/10.1038/s41467-023-37772-7.

(43) Chakkamalayath, J.; Hiott, N.; Kamat, P. V. How Stable Is the 2D/3D Interface of Metal Halide Perovskite under Light and Heat? *ACS Energy Lett.* **2023**, *8* (1), 169–171. https://doi.org/10.1021/acsenergylett.2c02408.

(44) Hoke, E. T.; Slotcavage, D. J.; Dohner, E. R.; Bowring, A. R.; Karunadasa, H. I.; McGehee, M. D. Reversible Photo-Induced Trap Formation in Mixed-Halide Hybrid Perovskites for Photovoltaics. *Chem Sci* **2015**, *6* (1), 613–617. https://doi.org/10.1039/c4sc03141e.

(45) Stolterfoht, M.; Wolff, C. M.; Márquez, J. A.; Zhang, S.; Hages, C. J.; Rothhardt, D.; Albrecht, S.; Burn, P. L.; Meredith, P.; Unold, T.; Neher, D. Visualization and Suppression of

Interfacial Recombination for High-Efficiency Large-Area Pin Perovskite Solar Cells. *Nat. Energy* **2018**, *3* (10), 847–854. https://doi.org/10.1038/s41560-018-0219-8.

(46) Qi, F.; Deng, X.; Wu, X.; Huo, L.; Xiao, Y.; Lu, X.; Zhu, Z.; Jen, A. K.-Y. A Dopant-Free Polymeric Hole-Transporting Material Enabled High Fill Factor Over 81% for Highly Efficient Perovskite Solar Cells. *Adv. Energy Mater.* **2019**, *9* (42), 1902600. https://doi.org/10.1002/aenm.201902600.

(47) Yang, Y.; Liu, C.; Ding, Y.; Arain, Z.; Wang, S.; Liu, X.; Hayat, T.; Alsaedi, A.; Dai, S. Eliminating Charge Accumulation via Interfacial Dipole for Efficient and Stable Perovskite Solar Cells. *ACS Appl. Mater. Interfaces* **2019**, *11* (38), 34964–34972. https://doi.org/10.1021/acsami.9b11229.

(48) Qiu, C.; Wagner, L.; Liu, J.; Zhang, W.; Du, J.; Wang, Q.; Hu, Y.; Han, H. Probing Charge Carrier Dynamics in Metal Halide Perovskite Solar Cells. *EcoMat* **2023**, *5* (1), e12268. https://doi.org/10.1002/eom2.12268.

(49) Lim, V. J.-Y.; Knight, A. J.; Oliver, R. D. J.; Snaith, H. J.; Johnston, M. B.; Herz, L. M. Impact of Hole-Transport Layer and Interface Passivation on Halide Segregation in Mixed-Halide Perovskites. *Adv. Funct. Mater.* **2022**, *32* (41), 2204825. https://doi.org/10.1002/adfm.202204825.

(50) Du, Y.; Tian, Q.; Wang, S.; Yang, T.; Yin, L.; Zhang, H.; Cai, W.; Wu, Y.; Huang, W.; Zhang, L.; Zhao, K.; Liu, S. (Frank). Manipulating the Formation of 2D/3D Heterostructure in Stable High-Performance Printable CsPbI3 Perovskite Solar Cells. *Adv. Mater.* **2023**, *35* (5), 2206451. https://doi.org/10.1002/adma.202206451.

(51) Meng, R.; Li, C.; Shi, J.; Wan, Z.; Li, Z.; Zhi, C.; Zhang, Y.; Li, Z. Reductive 2D Capping Layers through Dopamine Salt Incorporation for Pb–Sn Mixed Perovskite Solar Cells. *ACS Energy Lett.* **2023**, *8* (12), 5206–5214. https://doi.org/10.1021/acsenergylett.3c02039.

TABLE OF CONTENTS GRAPHIC